Estimation of optimum density and temperature for maximum efficiency of tin ions in *Z* discharge extreme ultraviolet sources

Majid Masnavi, Mitsuo Nakajima, Eiki Hotta, and Kazuhiko Horioka
Department of Energy Sciences, Tokyo Institute of Technology, 4259 Nagatsuta, Midori-ku, Yokohama 226-8502, Japan

Gohta Niimi
Gotenba Division, Ushio, 1-90 Komakado, Gotenba, Shizuoka 412-0038, Japan

Akira Sasaki
Advanced Photon Research Center, Japan Atomic Energy Research Institute, Kyoto 619-0215, Japan

(Received 11 October 2006; accepted 7 December 2006; published online 14 February 2007)

Extreme ultraviolet (EUV) discharge-based lamps for EUV lithography need to generate extremely high power in the narrow spectrum band of 13.5 ± 0.135 nm. A simplified collisional-radiative model and radiative transfer solution for an isotropic medium were utilized to investigate the wavelength-integrated light outputs in tin (Sn) plasma. Detailed calculations using the Hebrew University-Lawrence Livermore atomic code were employed for determination of necessary atomic data of the Sn^{4+} to Sn^{13+} charge states. The result of model is compared with experimental spectra from a Sn-based discharge-produced plasma. The analysis reveals that considerably larger efficiency compared to the so-called efficiency of a black-body radiator is formed for the electron density $\simeq 10^{18}$ cm^{-3}. For higher electron density, the spectral efficiency of Sn plasma reduces due to the saturation of resonance transitions. © *2007 American Institute of Physics*.
[DOI: 10.1063/1.2434987]

I. INTRODUCTION

Pulsed-power generator-based *Z* discharge plasmas have proved to be an effective radiation source in the x-ray and extreme ultraviolet (EUV) spectrum regions. The latter case is of great commercial interest because it is the extension of today's optical lithography toward a shorter wavelength.[1–4] In spite of impressive progress in the development and modeling of discharge EUV sources over the last several years,[4–13] only tin (Sn) plasma demonstrated large conversion efficiency (CE) of input power to emission in 2% bandwidth (± 0.135 nm) centered at the wavelength $\lambda = 13.5$ nm, the so-called in-band radiation. On the other hand, failure in heat removal from a discharge tube at high input power level that is required in EUV lithography application,[14] dictates us further investigation toward optimization of CE. Though there are many experimental results on Sn, however, calculation efforts to find out optimal region of electron density (n_e) and electron temperature (T_e) for maximizing CE in conditions relevant to discharge plasmas have not been reported.

In this article, in order to investigate the characteristics of CE in nonlocal thermodynamic equilibrium (non-LTE) Sn plasma, we have calculated level populations and line intensities of various transitions in the $Sn^{(4-13)+}$ charge states, by using a simplified collisional-radiative model (CRM) and a solution of radiative transfer equation, for the values ranging from $n_e = 10^{17}$ to 10^{20} cm^{-3} and $T_e = 20-60$ eV. This temperature range has been considered because the maximum efficiency of a black-body radiator is expected to be near the temperature T (eV) $\simeq 320/\lambda$ (nm).[15]

A computational model and assumptions are described briefly in Sec. II. The calculation results are presented and discussed in Sec. III, for conditions, which are relevant to discharge plasmas. This is followed by the conclusions.

II. CALCULATION MODEL AND ASSUMPTIONS

Under LTE hypothesis, the radiation of thermal light sources is governed by the fundamental laws of thermodynamics. Their intensity and spectral distribution, which depend on temperature, can be determined with the Kirchhoff's law of absorption-emission and the Planck's equation, respectively. In radiometry,[15–17] the Planck's equation (i.e., the line source function of S_λ) in a spectral radiance form L_λ^{LTE} (W cm^{-2} sr^{-1} nm^{-1}) is

$$L_\lambda^{\mathrm{LTE}} = S_\lambda^{\mathrm{LTE}} = \frac{2hc^2}{\lambda^5} \frac{1}{\exp(hc/\lambda k_B T) - 1}, \tag{1}$$

where h is the Planck's constant, c is the light speed, k_B is the Boltzmann's constant, and T is the temperature. The Planck's equation describes the thermodynamic limit: No object at a given temperature can emit more. L_λ^{LTE} is linked to the spectral exitance M_λ^{LTE} (W cm^{-2} nm^{-1}) by using the Lambert's cosine law as $M_\lambda^{\mathrm{LTE}} = \pi L_\lambda^{\mathrm{LTE}}$.[17] For a truly blackbody over the wavelength range from zero to infinity, the radiation power emitted by the surface is given by the Stefan-Boltzmann's law: $\int_0^\infty M_\lambda^{\mathrm{LTE}} d\lambda = \sigma T^4$ (W cm^{-2}), where σ is the Stefan-Boltzmann's constant. The efficiency of a blackbody radiator in the spectrum range of $d\lambda$ is given by[15]

$$\eta^{\mathrm{LTE}}(\text{in } 4\pi\text{sr}) = \frac{\int_{d\lambda} M^{\mathrm{LTE}}_{\lambda'} d\lambda'}{\sigma T^4}. \tag{2}$$

A necessary but not sufficient condition due to Griem, Wilson, or McWhirter,[18] for a plasma to be in LTE situation (viz., when the collision rate is significantly larger than the radiative decay rate, consequently, populations become distributed according to the Boltzmann's distribution function), yields a constraint as $n_e \gtrsim 10^{14}\sqrt{T_e}\chi^3$ (cm^{-3}). Here T_e and the excitation energy between two levels (χ) are in electron volt units. For example, assuming T_e=25 eV and χ=62–124 eV corresponding to the transition wavelengths over the range λ=20–10 nm, one gets $n_e \gtrsim (1-10)\times 10^{20}$ cm^{-3} to satisfy a necessary LTE condition. Thereby in a low-density region relevant to conditions in discharge plasmas, we expect that non-LTE effects play an important role on population distribution of excited states. In addition, level kinetics is strongly influenced by radiation transport. It is very difficult to carry numerical calculation of radiation transport without significant simplification of the problem due to the large number of spectral lines in Sn plasma.

For a fixed plasma depth, the integrated spectral radiance (ISR in watt/square centimeter steradian units) emerging in the normal direction from a slab medium with an assumed spatially constant source function is given by the area under emission spectral line as

$$\mathrm{ISR}_\lambda = S_\lambda W_\lambda = S_\lambda \int_{\mathrm{line}} [1 - \exp(-\tau_{\lambda'}\phi_{\lambda'})] d\lambda', \tag{3}$$

where W_λ is the equivalent linewidth, τ is the line center optical depth, and ϕ is the line profile function. The equivalent width of a spectral line as a function of optical depth (i.e., the curve of growth) is commonly used in astrophysical spectroscopic analysis[19] or in the laboratory plasmas for the determination of the total radiance, strengths, and width of isolated spectral lines.[16,20–26] A Voigt profile, which includes collisional and Doppler broadening was used in computing the curve of growth. We ignored natural line broadening, which becomes important only at extremely low temperature and densities. Due to the difficulty in the calculation of W_λ for the Voigt line shape, various simple analytical expressions for W_λ are usually employed and published.[27] Among expressions, which are accurate for a wide range of mixing parameter (a-parameter) values[27] are those given by Hansen and McKenzie[28] as

for $a < \pi/4$,

$$\frac{W_\lambda}{\Delta\lambda_D} = 2b\left[\exp\left(\frac{-a\tau_D}{\sqrt{\pi}b^2}\right) - \exp\left(\frac{a\tau_D}{\sqrt{\pi}b^2} - \frac{\sqrt{\pi}\tau_D}{2b}\right)\right] + 2\sqrt{a\sqrt{\pi}\tau_D}\,\mathrm{erf}\left[\sqrt{\frac{a\tau_D}{\sqrt{\pi}b^2}}\right], \tag{4}$$

where

$$b = \sqrt{\ln[\exp(\pi/4) + \tau_D]},$$

and for $a \geq \pi/4$,

$$\frac{W_\lambda}{\Delta\lambda_D} = 2\sqrt{a\sqrt{\pi}\tau_D}\,\mathrm{erf}\left[\sqrt{\frac{\pi^{3/2}\tau_D}{16a}}\right], \tag{5}$$

where τ_D is the optical depth in the center of Doppler profile,[29] erf is the error function, and $a = \sqrt{\ln 2}(\Delta\lambda_L/\Delta\lambda_D)$ is the Voigt parameter. Here, $\Delta\lambda_L(\Delta\lambda_D)$ is the full width at half maximum (FWHM) of the Lorentz (Doppler) profile line.

The semiempirical formula for the electron impact broadening (w_{se}) presented by Griem[30] is used to estimate $\Delta\lambda_L$ through the expression $\Delta\lambda_L = (w_{se}\lambda^2\pi c)$ as

$$\left(\frac{\Delta\lambda}{\lambda}\right)_L = 4.12\times 10^{-26}\frac{\lambda n_e}{\sqrt{T_e}}(\langle i|r^2|i\rangle + \langle j|r^2|j\rangle), \tag{6}$$

where the matrix elements of r^2 are given by

$$\langle m|r^2|m\rangle = \frac{n_m^2}{2(z+1)^2}[5n_m^2 + 1 - 3l_m(l_m+1)],$$

where n_m and l_m are the effective quantum numbers of the upper and lower states and z is the charge number of the level under consideration. In Eq. (6), n_e is in cubic centimeters, T_e in electron volts, and λ in nanometer units.

Equation (3) for ISR (i.e., the power per unit area, per unit solid angle, integrated over opacity-broadened Voigt profile line in watt/square centimeter steradian units) of a transition can be rewritten as

$$\mathrm{ISR}^{q+}_\lambda = \frac{C}{\lambda^4_{ji}}\left(\frac{g_j n_i^{q+}}{g_i n_j^{q+}} - 1\right)^{-1}\left(\frac{W_{\lambda_{ji}}}{\lambda_{ji}}\right), \tag{7}$$

where g_i and g_j are the statistical weights, n_i^{q+} and n_j^{q+} are the level population densities between the lower level i and the upper level j in ion with charge $q+$, respectively, and $C = 2hc^2 \simeq 1.19\times 10^{16}$ for λ in nanometer units.

To estimate population distributions, the set of rate equations (time-independent CRM) for density n_i^{q+} can be written as

$$\frac{d}{dt}n_i^{q+} = n_e\sum_{j\neq i} n_j^{q+}Q_{ji}(T_e) + \sum_{j>i} n_j^{q+}\psi_{ji}A_{ji} - n_i^{q+}\left[n_e\sum_{j\neq i} Q_{ij}(T_e) + \sum_{j<i}\psi_{ij}A_{ij}\right] = 0, \tag{8}$$

where $Q(T_e)$ represents the rate coefficient for electron-impact excitation or deexcitation as a function of T_e. The excitation rate coefficient is approximated by a modified Coulomb-Born formula for electric dipole transition,[29] and the deexcitation rate coefficient is obtained using detailed-balance relation. The opacity effect (i.e., reabsorption) on all of the level populations is estimated using the static optical depth at the line center of a Voigt profile. The effect of opacity on level population is calculated by reducing the radiative decay rate (A) by a factor equal to the Voigt profile escape factor (ψ) using a simple analytical formula as[22]

$$\psi = \frac{1+[\tau_V/(2+\tau_V^2)]}{1+\tau_V[\pi \ln(1+\tau_V)]^{1/2}} + [\pi V(0,a)]^{1/2} \times \frac{100a\tau_V}{1+100(a^{1/2}\tau_V + a\tau_V^{1/2})} \frac{1+[\tau_V(2+\tau_V^2)]}{1+(\pi\tau_V)^{1/2}}, \quad (9)$$

where $\tau_V = \tau_D \exp(a^2)\mathrm{erfc}(a)$ is the optical depth in the center of Voigt profile, erfc is the complementary error function, and the Voigt function in line center is given by

$$V(0,a) = \frac{1}{\pi^{1/2}(1+\pi a^2)^{1/2}}\left[1 - \frac{a}{\pi^{1/2}(1+\pi a^2)}\right].$$

The CRM calculations typically involved all of the electric dipole transitions among the most important $4d^k$, $4d^{k-1}nl$, $4d^{k-2}4fnl$, and $4p^5 4d^k nl$ configurations with the principal quantum number n of the excited electron up to five and the orbital quantum number l up to three in the $Sn^{(4-13)+}$ ions using detailed atomic data obtained from the Hebrew University-Lawrence Livermore atomic code (HULLAC).[31] Here k is the electron occupation number in the $4d$ shell, for example, $k=5$ in the case of Sn^{9+}. The effect of configuration interaction between the $4d^k$, $4d^{k-1}4f$, $4d^{k-1}5p$, $4d^{k-1}5f$, and $4p^5 4d^k$ states has been taken into account.[10]

In Eq. (8), we actually calculate the relative level populations,[32,33] namely, $m_j^{q+} = n_j^{q+}/n^{q+}$, where n^{q+} represents the total (summed over all of the levels of ion under investigation) number density $q+$ ion. The population density of each level is related to ionization balance by writing

$$n_j^{q+} = \frac{n_j^{q+}}{n^{q+}} \frac{n^{q+}}{n_i} \frac{n_i}{n_e} n_e = \frac{n_j^{q+}}{n^{q+}} \frac{\delta^{q+}}{\bar{Z}} n_e, \quad (10)$$

where we use the plasma neutrality condition: $n_e = \bar{Z}\, n_i$. Here n_i is the total ion density, $\bar{Z}$ is the average ionic charge state, and δ^{q+} is the fractional abundance of $q+$ ion. The fractional abundances at given T_e and n_e were found using steady-state ionization balance as

$$\frac{\delta^{(q+1)+}}{\delta^{q+}} = \frac{S_{q+}}{T_{(q+1)+}}, \quad (11)$$

where $T_{q+} = R_{q+} + C_{q+}$ is the total recombination term, which is considered in the calculation. Here S_{q+}, R_{q+}, and C_{q+} are, respectively, the electron collisional ionization, radiative, and three-body recombination rate coefficients of ion $q+$. In a discharge-produced plasma, the fractional abundances may be estimated using the rate coefficients introduced in the model of Colombant and Tonon,[34] as discussed in Refs. 11 and 35.

In Z discharge, a high-energy-density plasma is formed by an electromagnetic implosion accompanied by a shock wave. At the final phase of implosion, the plasma temperature increases rapidly due to the thermalization of kinetic energy that is considered as a dominant heating process, under a condition of almost constant total ion density. The electrons are heated by hot ions to the required temperatures, and subsequently the plasma decays due to the hydrodynamic expansion.[13,36,37] To estimate optimum n_e and T_e region for maximum CE, we consider a simple energy balance equation of the following form[38]

$$E_J + E_K = E_I + R_Y + E_P, \quad (12)$$

where E_J and E_K are, respectively, joule and kinetic energies coupled into the pinched plasma, E_I is the plasma internal energy, and E_P contains energy losses in neglected processes such as radiation from low-charge states before pinching (i.e., maximum compression) time and residual kinetic energy in the plasma rebound following peak compression. In Eq. (12), R_Y (in joule units) is radiated yield by defining an effective radiation time, which is expected to be in the order of the inertial confinement time. In the present work, we assumed that $E_J = E_P$. This assumption is effectual, at least, until a significant hydrodynamic expansion takes place. Because when the plasma is compressed by the azimuthal magnetic field generated by the induced current in the skin layer, it is also heated mainly by joule heating and radiative cooling occurs at the same layer. On the other hand, joule heating plays an important role at the pinching phase since plasma is in the resistive regime with a small radius. Under the aforementioned assumption, a figure of merit for CE is defined to optimize plasma conditions as[12,25,39]

$$\mathrm{CE\ (in\ } 4\pi\mathrm{sr)} = \Gamma \times \frac{\sum_{q+}\sum_{\lambda 2\%} \pi\, \mathrm{ISR}_\lambda^{q+} S_p \Delta\tau}{\sum_{q+}\sum_{\lambda} \pi\, \mathrm{ISR}_\lambda^{q+} S_p \Delta\tau + E n_i V_p}, \quad (13)$$

where $\lambda 2\%$ denotes the transitions in 2% bandwidth centered at $\lambda = 13.5$ nm, S_p, and V_p are plasma surface and volume, respectively, $\Delta\tau$ is emission duration, and E is defined as the minimum energy needed to heat and ionize a plasma to a given ionization state (E_I/atom) and the cohesive energy [$E_c = 3.14$ eV/atom for Sn (Ref. 40)] as

$$E = \sum_{j=1}^{\bar{Z}} I^j + \frac{3}{2}T_i + \frac{3}{2}\bar{Z}T_e + E_c, \quad (14)$$

where I is the ionization potential and T_i is the ion temperature. Note that, the first term of denominator in Eq. (13) characterizes the radiated yield. In Eq. (13), it is assumed that the electrical coupling efficiency[12,41,42] from pulsed-power generator to the internal plasma energy: $\Gamma = 1$. In other words, we restricted our analysis to inherent CE of Sn plasma.

III. RESULTS AND DISCUSSION

When a plasma is assumed to be in LTE situation, the level populations for each species depend entirely upon the plasma temperature and electron pressure and are given by Saha-Boltzmann's distribution. In general, the LTE assumption is a matter of computational convenience and is not expected to be valid in most cases, especially in the optically thin region relevant to discharge-based EUV sources. However, the efficiency of a steady-state blackbody source gives us an estimate on the maximum attainable or limiting level of CE for a sufficiently opaque plasma in energy-balance condition. The efficiency (η^{LTE}), the total in-band intensity, and the total radiation loss of a blackbody source versus plasma temperature (T) are shown in Fig. 1. Please note that in fact η^{LTE} is the spectral efficiency of a steady-state black-

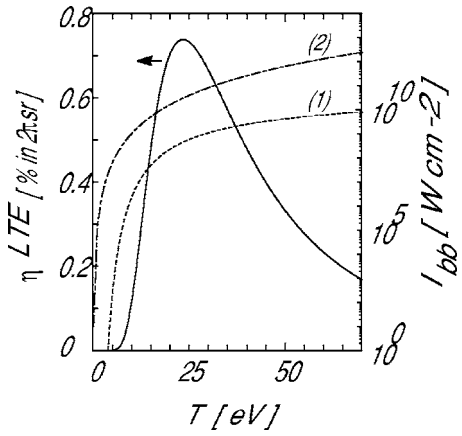

FIG. 1. Solid line: the in-band efficiency (η^{LTE}) of a steady-state black-body radiator. (1) Dashed line: $\int M_{\lambda'}^{\mathrm{LTE}} d\lambda'$ over the in-band region (I_{bb}: right ordinate). (2) Dashed-dotted line: σT^4 (I_{bb}: right ordinate).

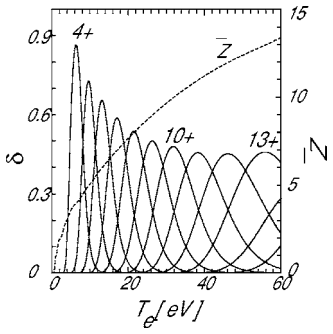

FIG. 2. Ion fractional abundances (δ: solid lines) and the average ionic charge state ($\bar{Z}$: dashed line) of a steady-state Sn plasma vs T_e at $n_e=5\times10^{18}$ cm^{-3} evaluated using the Colombant and Tonon's model.

body radiator and it reaches a maximum of $\simeq$0.74 (percent in 2πsr) at a temperature $T\simeq23.5$ eV a somewhat higher than a temperature in which results in the Wien's law ($k_BT=250/\lambda_{\max}$ eV nm$\simeq$18.5 eV).

As stated in Sec. II, the ionization charge states in non-LTE Sn plasma as shown in Fig. 2, were estimated from the Colombant and Tonon model,[34] which is based on the approximation that the steady-state rate equations couple only the ground state of adjacent ion stage. Within our temperature and density range, the small effect of the ionization potential lowering $\Delta\simeq2.7\times10^{-10}\sqrt{n_eT_e}$ eV cm^{-3} proposed by Griem[43] has been taken into consideration. Figure 2 shows that the dominant fractional abundance of the $Sn^{(9-13)+}$ ions at a given T_e is less than 50% of the total ion distribution. Although the model does not include the effect of excited states and dielectronic recombination, the ionization charge states are approximately in good agreement with a sophisticated calculation as discussed in Ref. 10, under the conditions of interest here.

To find out the in-band emission characteristics, a theoretical spectrum is calculated by weighting the detailed spectra with the fractional ion distribution. The typical stem representations of the ISR (W cm^{-2} sr^{-1}) versus λ in Sn plasma, including the $Sn^{(4-13)+}$ charge states are, respectively, presented in Figs. 3(a) and 3(b), for a constant $T_e=26$ eV at different electron densities of $n_e=10^{18}$ and 10^{19} cm^{-3}. Also, Figs. 3(c) and 3(d) illustrate the temperature dependence of ISR at constant $n_e=5\times10^{18}$ cm^{-3} for $T_e=20$ and 30 eV, respectively. To estimate opacity effect on the level populations, the set of nonlinear statistical equilibrium equations [Eq. (8)] is solved by iterations using the optically thin populations obtained as input parameters. The convergence from initial optically thin populations to equilibrium solution was obtained within three iterations. It is assumed that the photon path length ($R=0.04$ cm) is constant. It should be noticed that the opacity effects are separately calculated for different ions. Therefore, the overlaps of spectral lines arising from different charge states are not take into account in the model. To provide a clear picture of spectra, each stem diagram of ISR has been convoluted by a Gaussian profile of 0.02 nm

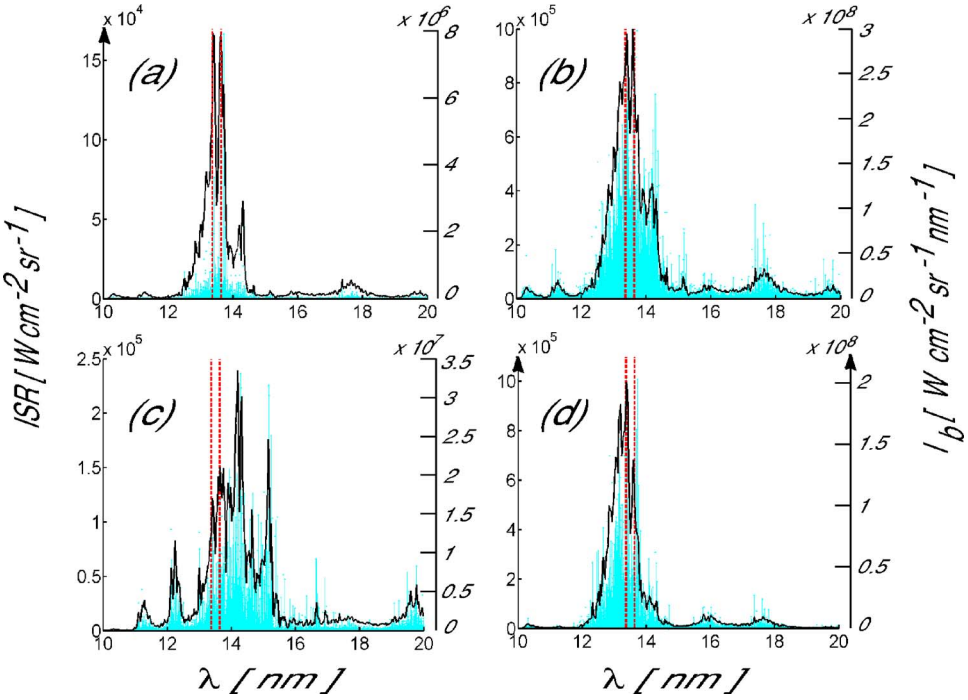

FIG. 3. Gray lines: stem representations of integrated spectral radiance ISR (W cm^{-2} sr^{-1}) over line profile of Sn plasma (left ordinate) vs λ. Black curve: I_b (right ordinate, in W cm^{-2} sr^{-1} nm^{-1} units) shows ISR after convolution with a Gaussian profile of 0.02 nm full width at half maximum. The in-band region (dashed line) is shown as a reference. The opacity effect is calculated for a plasma depth (radius) of $R=0.04$ cm. The spectrums are calculated at constant $T_e=26$ eV with different electron densities of (a) $n_e=10^{18}$ and (b) $n_e=10^{19}$ cm^{-3}. And constant $n_e=5\times10^{18}$ cm^{-3} for different (c) $T_e=20$ and (d) $T_e=30$ eV. Please note that the ordinates are not in the same scales.

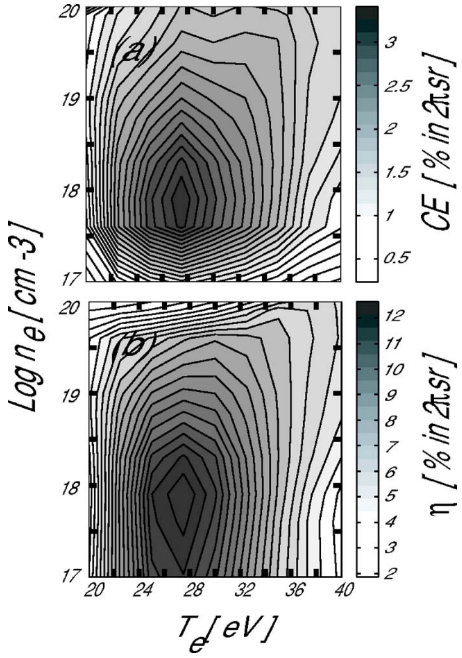

FIG. 4. (a) Contour of CE vs n_e and T_e for a cylinder plasma with 0.08 cm in diameter and 0.4 cm long. (b) The spectral efficiency.

the full width at half maximum (FWHM) as seen in Fig. 3, which is designated by I_b (black curve: right ordinate) in watt/square centimeter steradian units. We calculated only the line emission spectra, because it has been shown that[11] the contributions of bound-free and free-free transitions are negligible for a Sn plasma with electron density less than $\simeq 10^{20}$ cm^{-3} in our range of temperature interest. Figure 3 shows one strong emission peak mainly corresponding to the 4*d*-4*f* and 4*p*-4*d* transition arrays, occurring at around in-band region (13.5 nm), which are overlapped for the Sn^{8+} to Sn^{10+} charge states. Spectra [see, for example, Fig. 3(b)] contains additional weak transition arrays, which originate from the 4*d*-5*p* in the Sn^{8+} to Sn^{10+} (around 20, 18, and 16 nm, respectively) and the 4*d*-5*f* transitions in the Sn^{8+} to Sn^{9+} (around 11 and 10 nm, respectively). The 4*d*-5*p* and 4*d*-5*f* transitions are weaker compared to the main peak and occur in the wavelengths outside the in-band region. Comparing Figs. 3(a) and 3(b) reveal that the weak transition arrays appear with relatively high intensities in high-density Sn plasma (or optically thick plasma). This is due to the fact that with increasing density the spectral intensity distribution for all of the transitions approach to their intrinsic spectral radiance.[17] With reducing T_e, the intensities of the several weak transition arrays originating from relatively lower charge states increase dramatically at the shorter (for example, the 4*d*-5*f* transition of the Sn^{7+} at $\simeq$12.5 nm) and the longer (the 4*d*-4*f* transition of the Sn^{7+} at $\simeq$15 nm) wavelength sides of the in-band region as can be seen with comparison of Figs. 3(c) and 3(d). These fairly well-separated and relatively weak transition arrays are good indicators for the ionization stages of Sn ions involved in plasma.

Figure 4(a) represents a contour of the CE versus n_e and T_e. Plasma conditions span for $n_e = 10^{17} - 10^{20}$ cm^{-3} and $T_e = 20 - 40$ eV, while keeping $R = 0.04$ cm constant. According to étendue limit ($\leq$3.3 mm^2 sr),[44] the plasma length (L) assumed to be 0.4 cm. In addition, it is assumed that $T_e = T_i$. In Z discharge type transient plasma $\Delta\tau$ in Eq. (13), is governed by: (i) the characteristic timescale of the plasma hydrodynamic behavior, and (ii) ionization (τ_i) and recombination times of given ionization state at pinching phase. Thereby, it is clear that a realistic modeling of the time-integrated CE would, in principle, require at least information about ionization dynamics of Sn plasma and the plasma temperature-density history. Such an approach is beyond the scope of this work, mainly because of the extremely complicated atomic physics. On the other hand, these calculations shift the focus of investigation to the two-dimensional magnetohydrodynamics (MHD) simulation.[13] However, the analysis of numerous experimental and theoretical results in Z discharge revealed that $\Delta\tau$ can be estimated using the radiation pulse full width at half maximum. Thereby to estimate $\Delta\tau$ in Fig. 4(a), we have considered shortest time among: (i) the time scale characteristic of the Bennett equilibrium, i.e., the mean Alfvén transit time ($\bar{\tau} = R/\bar{V}_A$, where $\bar{V}_A = \sqrt{1+\bar{Z}V_i}$ is the mean Alfvén velocity,[45] and $\bar{V}_i$ is the mean ion thermal velocity), (ii) ionization time of dominant ionization charge state at a given n_e and T_e ($\tau_i = 1/n_e S_i$, where S_i is the ionization rate coefficient), and (iii) the mean radiative cooling time [$\bar{\tau}_{co} = E_t/P$,[46] where $E_t = 3n_e(T_i/\bar{Z} + T_e)V_p/2$ is the thermal energies of ions and electrons for the aforementioned plasma volume V_p and the corresponding total power loss of P], i.e., the time that plasma needs to radiate away its thermal energy. Note that P takes into account the power loss due to the $Sn^{(14-15)+}$ ions based on unresolved transition arrays framework of the HULLAC. We ignored a possible contributions of the $Sn^{(14-15)+}$ to in-band region. For example, the values of $n_e = 10^{18}$ cm^{-3}, $T_e = T_i = 28$ eV, and $\bar{Z} = 9$ yield $\bar{\tau}_A \simeq 1.7 \times 10^{-8}$ s, $\tau_i \simeq 4 \times 10^{-7}$ s in which accounts only the electron collisional ionization rate from the ground state of the dominant charge state, i.e., the Sn^{9+}, and $\bar{\tau}_{co} \simeq 8 \times 10^{-9}$ s. Thus for this condition CE in Fig. 4(a) is estimated based on $\bar{\tau}_{co}$. Please note that here, $\bar{\tau}_{co}$ is calculated using the values of $E_t \simeq 0.015$ J and $P \simeq 1.85 \times 10^6$ W in 4πsr. A comparison between Figs. 2 and 4(a) reveal that the Sn^{9+} charge state is the best emitter at in-band region. The spectral efficiency (η), i.e., when E sets to zero in Eq. (13) is shown in Fig. 4(b). We expect that the CE as shown in Fig. 4(a) approaches η for a steady-state plasma in the energy-balance condition. Note that η also should be limited to the efficiency of a steady-state blackbody source in an extremely high-density region. However, the discrepancy between Figs. 1 and 4(b) comes from our CRM calculation. That is, we did not calculate the effect of radiation emitted from higher levels including doubly excited states, free-free, and bound-free transitions as stated in Sec. II, which they could substantially reduce the η values in high-density region.

It should be noted that to estimate the CE and η, we used Eq. (3) in which there are two implicit assumptions behind that. First, it is assumed that the absorption and emission frequency profiles are identical, i.e., the line source function is not a frequency dependent (complete redistribution).[18] This is a common assumption, however, it requires that the

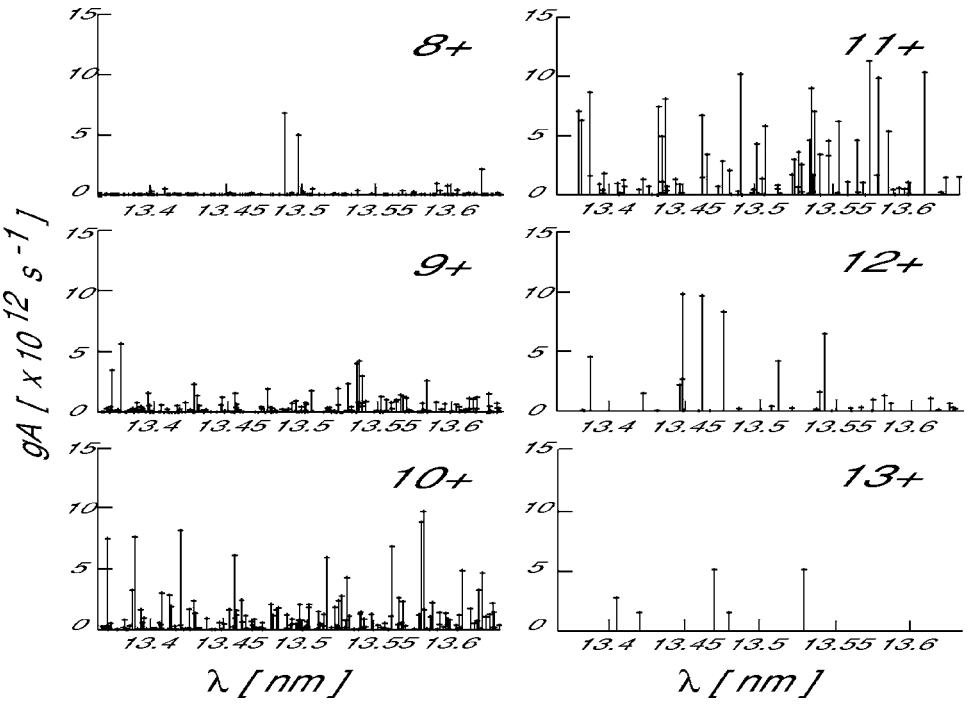

FIG. 5. Statistical weight (g_jA_{ji}) modeled spectra of the Sn^{8+} to Sn^{13+} charge states with the HULLAC code vs λ over the in-band region. The $4d$-$4f$ line positions are shifted to longer wavelength: for the Sn^{8+} (0.5 nm), Sn^{9+} (0.54 nm), $Sn^{(10-11)+}$ (0.49 nm), $Sn^{(12-13)+}$ (0.5 nm).

ion self-collision rate given by Spitzer (in numerical form by $\upsilon_i = 4.8\times10^{-8}\bar{Z}^4 n_i T_i^{-1.5}$ s^{-1} cm^{-3} eV under assumption of the Coulomb logarithm equal to $\ln\Lambda = 7$) be greater than the relevant radiative decay rate. Assuming $T_e = T_i = 26$ eV, $n_i = 2\times10^{17}$ cm^{-3}, and $\bar{Z} = 9$, one gets $\upsilon_i \simeq 5\times10^{11}$ s^{-1}. On the other hand, the average radiative decay rates of strong transitions inside the in-band region, for example, in the case of Sn^{9+}, is $\simeq 5\times10^{11}$ s^{-1}. Therefore, for the aforementioned conditions and lower density, the assumption of complete redistribution is somewhat questionable. Second, it is the assumption of a constant source function. In this case, the line can never be self-reversed, as is commonly observed in laser-produced Sn plasmas,[47,48] with very large optical depths. In this case, the line profile becomes flat topped with the FWHM measures by W_λ, in our calculation. Self-reversal occurs because the source function in a real situation is less at the boundaries than deep in the plasma, and for sufficiently large optical depth at line center the intensity in the wings of the line can be larger than at line center. The assumption of the constant source function, strictly speaking, is a physically incorrect approximation, because the populations of the upper states of resonance lines must be less at the boundaries of the plasma than near its center because the photon escape probability (ψ) at points on the plasma boundary is unity. We can account for the decrease of the source function at the boundary, by taking the worst possible case, i.e., assume a layer at the boundary for which the optical depths, and consequently, ISR_λ are zero. Assuming that the ISR_λ and τ_D have their maximum values at the center of a plasma cylinder having radius R and decrease linearly toward both plasma edges. That is, to estimate population distributions using Eq. (8), the half-value of τ_D is used to estimate the escape probability factor of ψ and also the equivalent linewidth of W_λ. We found that optimum region of n_e for maximizing the CE and η in Fig. 4 does not change significantly. For example, the optimum n_e for the CE in Fig. 4(a) shifts (less than two times) to the higher-density region and its maximum value reduces to $\simeq 3$ (percent in 2πsr). The reason might be explained by the nature of the curve of growth. Generally, the curve of growth consists of three parts: (i) linear, (ii) saturated, and (iii) square root behaviors in which depends on the Voigt parameter (i.e., pressure broadening).[16] The optimum region of n_e for the CE and η occurs in saturated phase of resonance lines and the Voigt parameters of the Sn lines are small in this region ($\tau_V \simeq \tau_D$). For example, assuming $T_e = 27$ eV, $n_e = 10^{18}$ cm^{-3}, average Voigt parameters of transitions inside the in-band region is $\bar{a} \simeq 0.007$. Thereby, a somewhat reduced optical depth does not change significantly the optimum region of n_e in Fig. 4.

Comparison of our calculated spectrum with experimental results revealed that on average, different shifts would have to be applied to different calculated configurations in order to achieve good agreement. For example, with a global displacement of 0.15 nm to longer wavelength, the calculated spectrum has agreement with experiments. However, the precise positions of the emission lines are important in the EUV lithography application.

According to the recent experimental results of Sn spectra excited in vacuum spark,[49] and also by comparison the charge-exchange spectroscopy results and HULLAC data,[50,51] we did a correction ($\simeq$0.5 nm global displacement of calculated spectrum toward longer wavelength) on the emission line positions. Figure 5 shows the g_jA_{ji} (the statistical weight of upper state times the radiative decay rate) modeled spectra of the Sn^{8+} to Sn^{13+} charge states using the HULLAC code versus λ over the in-band region. Based on the aforementioned experimental results the $4d$-$4f$ line positions are shifted toward a longer wavelength. A comparison between Fig. 5 and the classified lines of Sn plasma in Fig. 3 as discussed in Ref. 49, shows a satisfactory agreement on the number of transitions and line positions. Nevertheless, this is a rough comparison because the line intensities are

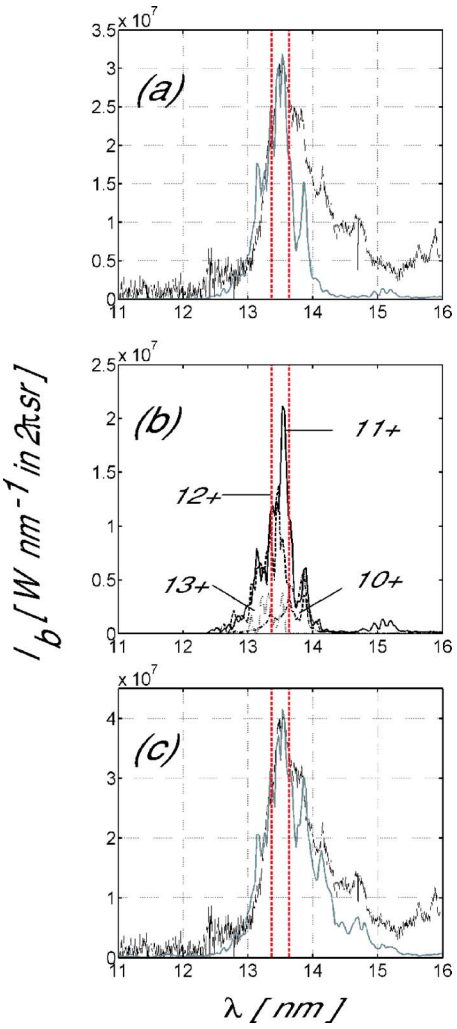

FIG. 6. (a) An experimental spectrum (black curve) of Sn-based *Z* discharge plasma in comparison to the calculated spectra (gray curve) vs λ. A homogeneous cylinder plasma with 0.06 cm in diameter and 0.4 cm long, $n_e=5\times10^{18}$ cm^{-3}, and $T_e=42$ eV is assumed. (b) The line radiation contributions of the main individual ions. (c) Two calculated spectra are added for the same conditions of (a), but at two different electron temperatures of $T_e=27$ and 42 eV. The in-band region (dashed line) is shown as a reference.

proportional to line strengths or g_jA_{ji} values only in sufficiently high-density plasma, when the population of excited states approaches a Boltzmann's distribution. In low-density plasmas, the level populations and consequently the line intensities also depend on the excitation rates of ions.

Figure 6(a) represents a typical experimental spectrum (black curve) of Sn-based *Z* discharge plasma in comparison to the theoretical spectra (gray curve) calculated versus λ in the range from 11 to 16 nm. In addition, the most important contributions of the line emission of the individual ions to the calculated spectra is plotted in Fig. 6(b). It is found that the theoretical spectra fits the experimental results best when the electron density and temperature are set to be 5×10^{18} cm^{-3} and 42 eV, respectively. To calculate opacity effect, the plasma depth is set to be $R=0.03$ cm, approximately based on the experimental results. A discussion of the plasma diagnostic methods that lead to the recorded spectra is given in Ref. 52. The comparison of the experimental and theoretical spectra shows a good agreement only for the in-band region and shorter wavelengths. As Fig. 6(b) shows, the $Sn^{(10-13)+}$ charge states are the best emitters at the in-band region. The calculated spectra underestimates the radiation at the longer wavelength side, that is, radiation originating from lower charge states. Such a result may indicate that the whole emissive region is not at the same temperature, and thus it can be necessary to consider a multitemperature plasma. In general spectrum emitted by a Sn plasma composed of several ionization states is expected to be dependent on the fractional ion abundances. Moreover, in *Z* discharge transient non-LTE plasmas with strong temperature and density gradients, these abundances are space and time dependent and cannot be simulated under the assumption of perfect homogeneity of the plasma. We think that the major portion of photons in the longer wavelengths of the recorded spectrum are emitted during the transient expanding phase while the plasma is cooling and recombination processes dominate. For example, Fig. 6(c) illustrates a calculated spectra in comparison of the time-integrated experimental spectrum. We added the calculated spectrum as shown in Fig. 6(a) with other spectra at the same conditions, but for the lower electron temperature of $T_e=27$ eV. Figure 6(c) shows more agreement between the calculated and experimental spectra than Fig. 6(a).

With the improved line positions, we recalculated contour plots of the CE and η versus n_e and T_e as shown in Figs. 7(a) and 7(b), respectively. Plasma conditions are the same as Fig. 4, except T_e which span in the range of 20–60 eV. Also a contour of the total in-band power in logarithmic scale ($P_{2\%}$) versus n_e and T_e is shown in Fig. 7(c). A comparison between the optimum region of T_e ($\simeq$42 eV) for maximizing the CE and η in Figs. 7(a) and 7(b), and the fractional ion abundances in Fig. 2 reveal that the $Sn^{(11-12)+}$ charge states are best emitters at the in-band region.[53] Although the values of the CE and η as, respectively, shown in Figs. 7(a) and 7(b) are approximately twice of those calculated in Fig. 4, however, the optimum n_e region ($\simeq10^{18}$ cm^{-3}) is the same. The optimal region occurs in low density Sn plasma, where the total in-band power is low as can be seen in Fig. 7(c). It suggests that to enhance the CE and in-band power, it is crucially important to prolong emission duration of low density Sn plasma and/or to increase in the repetition rate of pulsed-power generator. It may be interesting to notice here that the maximum η of Sn-based discharge source is approximately half compared to that of lithium plasma.[54] It is important to note that the release of potential energy [see Eq. (14)] and its effect on the CE value is not considered in the article. In other words, it is assumed that only thermal energy of plasma can converts to radiation. However the ionization energy can be released in recombination phase of *Z* discharge plasma via photon radiation, and consequently enhance the CE. But a more exact calculation of the time-integrated CE would have to include the MHD model coupled to ionization dynamics in which such a study is in progress in our laboratory. At constant $T_e=42.5$ eV and the aspect ratio $L/R=4$, the CE calculated as a function of *R* over the range of 0.01–0.06 cm. It is found that the optimal region of density varies from $n_e\simeq4\times10^{17}$ cm^{-3} at $R=0.06$ cm to $n_e\simeq4\times10^{18}$ cm^{-3} in the case of $R=0.01$ cm

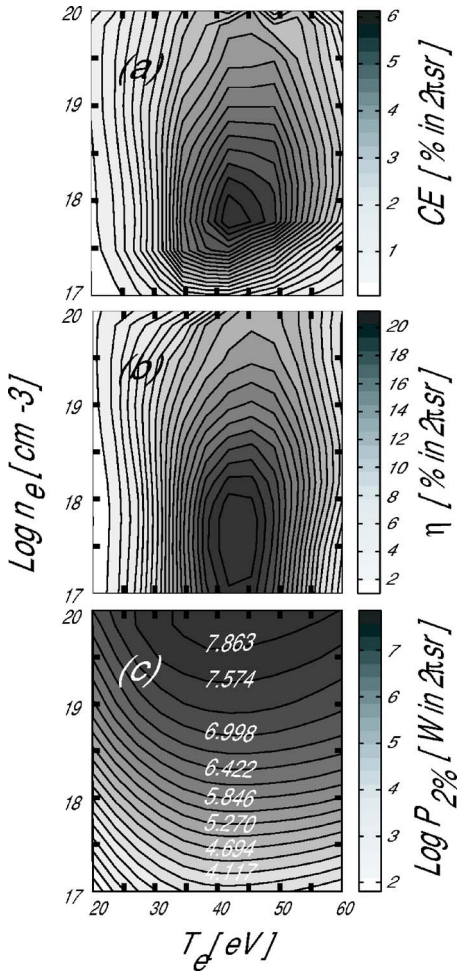

FIG. 7. (a) Contour of CE vs n_e and T_e for a cylinder plasma with 0.08 cm in diameter and 0.4 cm long. (b) The spectral efficiency. (c) The natural logarithm of total in-band power ($P_{2\%}$).

due to the larger collisional excitation rates from the lower to upper states and nonlinear effect of opacity on population distributions. In the latter case, the CE decreases to $\simeq 5.3\%$ in 2πsr. The optimal region of n_e occurs for conditions that the average of the optical depths in the center of Doppler profile for strong transition lines at the in-band region is $\simeq 1$. In other words, the Voigt parameter (a parameter) does not play an important role on the curve of growth in this region. Since the Voigt profile is obtained as a convolution of the Doppler and Lorentz radiation broadening profiles, the limits of the Voigt parameter $a \to 0$ and $a \to \infty$ correspond to a pure Doppler[24,25] and a pure Lorentz profile,[21,23] respectively. We recalculated the CE and η using a curve of growth and escape probability factor for a pure Doppler profile line. For cylindrical geometry, values of the Doppler profile escape factor have been calculated by Bhatia and Kastner,[55] and expressed for convenience as the logistic function $\psi \simeq \alpha_1/(1+\exp[\alpha_2(\log \tau_D - \alpha_3)])$, where for normal to cylindrical axis $\alpha_1 = 1.001\,079\,6$, $\alpha_2 = 2.321\,213\,6$, and $\alpha_3 = 0.223\,355\,45$. We found almost the same optimal region of n_e as shown in Figs. 7(a) and 7(b).

Note that the maximum CE in Fig. 7(a) occurs at $n_e \simeq 10^{18}$ cm^{-3} and $T_e \simeq 42$ eV in which is estimated based on $\Delta\tau = \bar{\tau}_{co} \simeq 7$ ns. For the aforementioned plasma conditions we have $E_t \simeq 0.023$ J and $P \simeq 3.2 \times 10^6$ W in 4πsr. Also the total internal energy [the second term in denominator of Eq. (13)] is $\simeq 0.053$ J. It may be interesting to find out a relationship between the CE and η in Z discharge plasma based on a simple analytical picture. The total energy coupled to plasma could be separated into an inductive and a resistive parts. To illustrate this, recall that the magnetic energy converted to the kinetic energy of the imploding plasma column is fairly estimated as $E_k = (\varepsilon I_m^2 L/c^2)\ln(R_i/R_f)$ in Gaussian units and in numerical form by $E_k = 5 \times 10^{-4} \varepsilon I_m^2 \Delta F$ J kA. Here L is the pinch length, R_i is the initial plasma radius, R_f is its final radius at pinching time, I_m is the peak current, $\Delta F = 2L \ln(R_i/R_f)$ nH cm is the change of the pinch inductance in the implosion, and ε is a dimensionless coefficient of order unity that accounts for the current pulse shape: $\varepsilon = 1$ for a constant current, and $\varepsilon \simeq 0.5$ for typical sinusoidal current pulse.[41] Assuming $R_i = 10 \times R_f$ (i.e., ten-times compression in which this assumption can be supported by experimental and numerical results) and the aforementioned plasma length, one gets $I_m \simeq 11$ kA to make such a plasma with the total internal energy of 0.053 J. The Sn plasma at the optimal condition of the CE as shown in Fig. 7(a) can radiate its thermal energy part during $\simeq 7$ ns. Note that this is the mean value due to the steady-state nature of the model. On the other hand, the joule heating in an unmagnetized plasma is $P_J = 900 \bar{Z} L R_f^{-2} \ln \Lambda T_e^{-1.5} I_m^2$ W cm eV kA. Assuming constant radius and current (i.e., the time-dependent Bennett equilibria[45]), the more coupled energy to the pinched plasma by joule heating in 7 ns is $\simeq 0.054$ J under assumption of $\ln \Lambda = 7$. This amount of joule heating is radiated during $P_J/P \simeq 17$ ns. This behavior shows that, when the amount of resistive heating is too large, the plasma cannot radiate couple energy fast enough to prevent its late time conversion into kinetic energy of E_P [see Eq. (12)]. We expect that the inherent CE as shown in Fig. 7(a) approaches η in the case of joule heating at the pinching phase due to the fact that the average ionic charge state is approximately constant. It should be stressed that although Bennett equilibrium is an ideal situation to enhance the inherent CE, however a critical issue might be energy loss to the electrodes. Therefore, a complete picture of Z discharge plasma and estimation of the absolute value of the CE of Sn plasma would require a full account of MHD behavior self-consistently coupled to the ionization dynamics, and plasma-surface interaction[13] including energy loss to the electrodes, which are beyond the scope of the present study.

IV. CONCLUSIONS

Using a simplified collisional-radiative model and a radiative transfer solution for an isotropic medium, we have calculated the emission spectra for tin plasma. The importance of opacity effect on the saturation of resonance lines has been studied based on the curve of growth analysis. As a figure of merit we calculated the inherent conversion and spectral efficiencies, which required us to optimize Z discharge parameters for enhancing 13.5 ± 0.135 nm radiation. The analysis reveals that larger efficiency compared to the so-called efficiency of a blackbody radiator is formed at the

electron density $\simeq 10^{18}$ cm^{-3} for the relevant plasma dimension of gas discharge-based EUV source. It is found that to enhance efficiency, it is crucially important to prolong emission duration of low-density Sn plasma and to operate plasma source at low-input power level. Thereby with the increase in the repetition rate of pulsed-power generator, an efficient high-power EUV light source in which is required for lithography can be achieved.

ACKNOWLEDGMENTS

This work was sponsored in part by the New Energy and Industrial Technology Development Organization (NEDO) and the Extreme Ultraviolet Lithography System Development Association (EUVA) of Japan.

[1] D. Attwood, *Soft X-Rays and Extreme Ultraviolet Radiation* (Cambridge, New York, 1999).
[2] W. T. Silfvast, IEEE J. Quantum Electron. **35**, 700 (1999).
[3] D. Bratton, D. Yang, J. Dai, and C. K. Ober, Polym. Adv. Technol. **17**, 94 (2006).
[4] See several contributions in *Proceedings of the EUV Source Workshop*, San Jose, CA, 27 February 2005 (Sematech, Austin, TX, 2005).
[5] M. A. Klosner, H. A. Bender, W. T. Silfvast, and J. J. Rocca, Opt. Lett. **22**, 34 (1997).
[6] N. Böwering, M. Martins, W. N. Partlo, and I. V. Fomenkov, J. Appl. Phys. **95**, 16 (2004).
[7] C. Jiang, A. Kuthi, M. A. Gundersen, and W. Hartmann, Appl. Phys. Lett. **87**, 131501 (2005).
[8] E. R. Kieft, J. J. A. M. van der Mullen, and V. Banine, Phys. Rev. E **72**, 026415 (2005).
[9] B. S. Bauer, V. Makhin, S. Fuelling, and I. R. Lindemuth, Proc. SPIE **6151**, 61513N (2006).
[10] A. Sasaki, K. Nishihara, F. Koike, T. Kagawa, T. Nishikawa, K. Fujima, T. Kawamura, and H. Furukawa, IEEE J. Sel. Top. Quantum Electron. **10**, 1307 (2004).
[11] M. Poirier, T. Blenski, F. de Gaufridy de Dortan, and F. Gilleron, J. Quant. Spectrosc. Radiat. Transf. **99**, 482 (2006).
[12] T. Krucken, K. Bergmann, L. Juschkin, and R. Lebert, J. Phys. D **37**, 3213 (2004).
[13] A. Hassanein, V. Sizyuk, V. Tolkach, V. Morozov, T. Sizyuk, B. J. Rice, and V. Bakshi, Proc. SPIE **5374**, 413 (2004).
[14] J. Jonkers, Plasma Sources Sci. Technol. **15**, S8 (2006).
[15] M. A. Bramson, *Infrared Radiation, A Handbook for Applications* (Plenum, New York, 1968), p. 68.
[16] T. Fujimoto, *Plasma Spectroscopy* (Clarendon, Oxford, 2004), Chaps. 2 and 8.
[17] F. Grum and R. J. Becherer, *Optical Radiation Measurements*, edited by F. Grum (Academic, New York, 1979), Vol. I, Chaps. 3 and 4.
[18] R. W. P. McWhirter, in *Plasma Diagnostic Techniques*, edited by R. H. Huddelstone and S. I. Leonard (Academic, New York, 1965).
[19] M. E. Foord, R. F. Heeter, P. A. M. van Hoof, R. S. Thoe, J. E. Bailey, M. E. Cuneo, H. K. Chung, D. A. Liedahl, K. B. Fournier, G. A. Chandler, V. Jonauskas, R. Kisielius, L. P. Mix, C. Ramsbottom, P. T. Springer, F. P. Keenan, S. J. Rose, and W. H. Goldstein, Phys. Rev. Lett. **93**, 055002 (2004).
[20] I. M. Vardavas, J. Quant. Spectrosc. Radiat. Transf. **49**, 119 (1993).
[21] S. O. Kastner and A. K. Bhatia, J. Quant. Spectrosc. Radiat. Transf. **58**, 217 (1997).
[22] M. H. Elghazaly, J. Quant. Spectrosc. Radiat. Transf. **90**, 389 (2005).
[23] G. Schriever, K. Bergmann, and R. Lebert, J. Appl. Phys. **83**, 4566 (1998).
[24] K. Bergmann, R. Lebert, and W. Neff, J. Phys. D **30**, 990 (1997).
[25] M. Masnavi, M. Nakajima, A. Sasaki, E. Hotta, and K. Horioka, Jpn. J. Appl. Phys., Part 1 **43**, 8285 (2004).
[26] Y. Andrew, I. Abraham, J. H. Booske, Z. C. Lu, and A. E. Wendt, J. Appl. Phys. **88**, 3208 (2000).
[27] S. O. Kastner, J. Quant. Spectrosc. Radiat. Transf. **54**, 1001 (1995).
[28] C. F. Hansen and R. L. McKenzie, J. Quant. Spectrosc. Radiat. Transf. **11**, 349 (1971).
[29] R. C. Elton, *X-Ray Lasers* (Academic, San Diego, CA, 1990), Chaps. 2 and 3.
[30] H. R. Griem, Phys. Rev. **165**, 258 (1968).
[31] A. Bar-Shalom, M. Klapisch, and J. Oreg, J. Quant. Spectrosc. Radiat. Transf. **71**, 169 (2001).
[32] D. E. Kim, D. S. Kim, and A. L. Osterheld, J. Appl. Phys. **84**, 5862 (1998).
[33] M. Masnavi, T. Kikuchi, M. Nakajima, and K. Horioka, J. Appl. Phys. **92**, 3480 (2002).
[34] D. Colombant and G. F. Tonon, J. Appl. Phys. **44**, 3524 (1973).
[35] J. White, P. Hayden, P. Dunne, A. Cummings, N. Murphy, P. Sheridan, and G. O'Sullivan, J. Appl. Phys. **98**, 113301 (2005).
[36] M. Masnavi, M. Nakajima, A. Sasaki, E. Hotta, and K. Horioka, Appl. Phys. Lett. **87**, 111502 (2005).
[37] K. T. Lee, D. E. Kim, and S. H. Kim, Phys. Rev. Lett. **85**, 3834 (2000).
[38] D. Mosher, N. Qi, and M. Krishnan, IEEE Trans. Plasma Sci. **26**, 1052 (1998).
[39] T. Aota and T. Tomie, Phys. Rev. Lett. **94**, 015004 (2005).
[40] A. Anders, Appl. Phys. Lett. **80**, 1100 (2002).
[41] J. Katzenstein, J. Appl. Phys. **52**, 676 (1981).
[42] S. Lee, J. Phys. D **16**, 2463 (1983).
[43] H. R. Griem, *Plasma Spectroscopy* (McGraw-Hill, New York, 1964).
[44] V. Banine and R. Moors, J. Phys. D **37**, 3207 (2004).
[45] M. A. Liberman, J. S. D. Groot, A. Toor, and R. B. Spielman, *Physics of High-Density Z-Pinch Plasmas* (Springer, New York, 1999).
[46] J. R. Peterson and A. C. Fabian, Phys. Rep. **427**, 1 (2006).
[47] S. Fujioka, H. Nishimura, K. Nishihara, A. Sasaki, A. Sunahara, T. Okuno, N. Ueda, T. Ando, Y. Tao, Y. Shimada, K. Hashimoto, M. Yamaura, K. Shigemori, M. Nakai, K. Nagai, T. Norimatsu, T. Nishikawa, N. Miyanaga, Y. Izawa, and K. Mima, Phys. Rev. Lett. **95**, 235004 (2005).
[48] Y. Tao, S. S. Harilal, M. S. Tillack, K. L. Sequoia, B. O'Shay, and F. Najmabadi, Opt. Lett. **31**, 2492 (2006).
[49] S. S. Churilov and A. N. Ryabtsev, Phys. Scr. **73**, 614 (2006).
[50] H. Tanuma, *Proceedings of the EUV Source Modeling Workshop* (International SEMATECH, Miyazaki, Japan, 2004).
[51] A. Sasaki, K. Nishihara, A. Sunahara, T. Nishikawa, F. Koike, K. Kagawa, and H. Tanuma, Proc. SPIE **6151**, 61513W (2006).
[52] Y. Teramoto, G. Niimi, D. Yamatani, Y. Joshima, K. Bessho, T. Shirai, T. Takemura, T. Yokota, H. Yabuta, K. Paul, K. Kabuki, K. Miyauchi, M. Ikeuchi, K. Hotta, M. Yoshioka, and H. Sato, Proc. SPIE **6151**, 615147 (2006).
[53] T. Kagawa, K. Nishihara, A. Sasaki, and F. Koike, J. Plasma Fusion Res. **7**, 245 (2006).
[54] M. Masnavi, M. Nakajima, A. Sasaki, E. Hotta, and K. Horioka, Appl. Phys. Lett. **89**, 031503 (2006).
[55] A. K. Bhatia and S. O. Kastner, J. Quant. Spectrosc. Radiat. Transf. **58**, 347 (1997).